A phase-field approach embedded in the Theory of Porous Media for the description of dynamic hydraulic fracturing

Wolfgang Ehlers [*], Chenyi Luo

Institute of Applied Mechanics (CE), University of Stuttgart, Pfaffenwaldring 7, 70569, Stuttgart, Germany

Highlights

- Featuring fracking processes based of the TPM and a phase-field fracture model.
- Using a fully coupled FEA for the fracturing solid and the pore-fluid flow.
- Numerical examples for 2- and 3-dimensional problems.

Abstract

Hydraulic fracturing is a big issue in the exploitation of oil and gas resources as well as in the production of heat in deep geothermal energy plants. Investigating hydraulic fracturing processes numerically by means of a finite-element analysis, one has to address the porous solid and its pore content within a fully coupled computational approach. For this purpose, the present article combines the well-established Theory of Porous Media with elements of fracture mechanics, especially, with the phase-field approach to fracture, which has proven as a successful tool for the computation of fracturing processes in the field of standard solid mechanics.

Although hydraulic fracturing is widely applied in practice, this procedure has not yet been investigated adequately by means of a full theoretical and computational framework on the basis of a multicomponent medium tackling a porous solid skeleton and its pore content with their mutual interaction of deformation and fracture, and fluid-driven processes both in the solid bulk and cracking domains. Addressing these features, the article concentrates on a permeable elastic solid skeleton, where the fracturing process is governed by brittle fracture driven either by a prescribed fluid pressure or by a prescribed fluid influx. Two- and three-dimensional numerical examples computed by use of the coupled solver PANDAS exhibit the possibilities of this approach.
© 2016 Elsevier B.V. All rights reserved.

Keywords: Phase-field theory; Theory of Porous Media; Hydraulic fracturing

* Corresponding author. Fax: +49 711 685 66347.
  E-mail addresses: Wolfgang.Ehlers@mechbau.uni-stuttgart.de (W. Ehlers), Chenyi.Luo@mechbau.uni-stuttgart.de (C. Luo).

1. Introduction

Hydraulic fracturing in porous media came into play in the late 1940s and found its application in oil and gas industries, the exploitation of deep groundwater sources and deep geothermal energy plants. Only after 1990, it was also applied for the exploitation of unconventional oil and gas resources such as shale gas. Hydraulic fracturing, also known as "fracking", is a common technique in oil and gas industries. The key point of this technique is to artificially create a system of fissures and cracks in oil- or gas-bearing strata by means of injecting a high-pressured fluid into a wellbore such that more dissolved or diffusive oil or gas is available in the outflow. For details about this process, the reader is referred, for example, to Bažant et al. [1].

In contrast to its popularity in commercial applications, the relevant design and control of fracking techniques is almost empirical, which may lead to severe consequences, such as the leakage of contaminants, high risk during manipulation and the destabilisation of the stratum. Although the demand of systematic and theoretical knowledge is urgent, the process of cognition is still at a nascent stage. The basic difficulty relies on the fact that two complex phenomena, namely fracturing and porous, multi-phasic and multi-component material, have to be handled simultaneously during the fracking process. In general, the former involves jumps in the continuity of the basic solid material, which might cause local instabilities of the structure and a succeeding lack of convergence of the numerical algorithm during simulation. In addition, the latter requires a real or a virtual homogenisation strategy of the overall aggregate, such that the microscopic structure of the solid skeleton and the pore fluids including the mutual interactions of the solid and fluid components are properly defined on the macroscopic scale. While in fracking, cracks are initiated and propagated by the fluid pressure, this, in turn, affects the fluid flow both in fissures and cracks and in the remainder of the overall domain. This involves the need of a numerical algorithm, which is able to handle the multi-component character of the overall aggregate and the cracking behaviour of the porous solid simultaneously.

In order to depict fracture in solids, Griffith [2] related its propagation to a so-called critical energy-release rate. This energy-oriented criterion sets up the foundation of the classical theory of brittle fracture, based on which successors of Griffith, such as Irwin [3] or Rice [4], developed various approaches for specific materials. Other than brittle fracture, materials may fail in different ways, thus leading to a distinction between brittle and ductile materials, where a representative of the former is rock and of the latter is steel. Distinct from brittle material, ductile material undergoes large irreversible deformations, especially, in the vicinity of the crack tip before initiation of a macroscopic crack. In order to describe the pre-crack performance of solids more precisely, Barenblatt [5] and Dugdale [6] independently introduced the cohesive zone model. To summarise all failure modes of solid materials, some researchers define them as "damage" and categorise them as brittle damage, ductile damage, creeping damage and fatigue damage. The basic ideas of damage mechanisms go back to Kachanov [7] and successors and were later elaborated, for example, by Gross [8], Lemaitre [9] and others. Damage models usually contain an additional scalar damage variable, which reduces the stiffness of the material during its evolution. However, standard damage models suffer from the loss of ellipticity of the governing differential equations and the strong dependency of the results on the mesh size.

All above-mentioned approaches try to describe the fracture by advancing the material model. In contrast, another possibility was found by characterising a new internal boundary introduced by the crack. In the framework of the Finite-Element Method (FEM), this led to the Extended Finite-Element Method (XFEM), compare Belytschko & Black [10], Möes & Belytschko [11] and Möes et al. [12], where the crack path is traced by additional shape functions. The advantage of this method is at the same time its drawback, since the XFEM needs to predict all possible crack modes by properly defined additional shape functions. For increasing problems, especially, under three-dimensional (3-d) conditions, this pre-setting of crack scenarios becomes complicated and computationally demanding.

In 1950, Ginzburg and Landau established the so-called Ginzburg–Landau theory to explain superconductivity. As an extended form of this approach, the so-called phase-field theory was later applied to phase-transformation problems, such as solidification, cf. Gurtin [13]. Only during the 1990s, the phase-field theory was found to be convenient for the application to fracture problems, compare, for example, the work of Francfort & Margio [14]. Similar to the standard damage model, the phase-field theory also includes an additional scalar variable, the order parameter, which, together with its gradient and other variables, such as strain or temperature, governs the state of the material. The phase-field theory can also be understood as an extended energetic approach of Griffith's theory. This has been considered by Kuhn & Müller [15], who showed the consistency of the phase-field approach for fracture to the classical Griffith's theory.

Although the application of the phase-field theory to fracture in solids is rather recent, this approach has received immediate attention, for example, by Borden et al. [16], Miehe et al. [17] or Kuhn & Müller [15]. In their work, the phase-field approach exhibits its outstanding performance in solving crack problems. In comparison to the XFEM and the damage model, the advantages of applying the phase-field theory can be summarised as follows:

(1) In case that there is no mesh refinement, the use of the phase-field approach maintains the finite-element mesh of the problem, thus not only saving computation time during the simulation but also yielding efforts when treating the possible crack modes in the theoretical derivation and the numerical implementation.

(2) The introduction of the gradient terms in the *Helmholtz* free energy of the solid makes the phase-field theory advantageous in comparison to the standard damage model, since it does not suffer from a pathological sensitivity of the numerical results towards the size of finite elements, cf. Jirásek [18].

Applying the phase-field approach to fracturing porous media, such as rock or soil, there is not only the solid material, but also the pore fluids have to be treated. This can be successfully done within the well-founded framework of the Theory of Porous Media (TPM). Porous media are not only of great interest since lots of decades, but they also exhibit a complex internal structure that has to be handled on the macroscopic scale. However, it is not astonishing that first approaches to treat porous media occurred when coastal protection structures had to be designed, where water had to be retained by permeable structures, such as dykes or embankments. For an historical review, compare, for example, de Boer [19] or Ehlers [20].

Tackling porous media, two basic continuum-mechanical approaches are competing, the Biot's approach [21–23] dating back to 1941, and the TPM basically established by Bowen [24,25] in 1980 and the school of de Boer [26,27] and Ehlers [28,29] starting around 1985. While the Biot's approach was established more or less intuitively, the TPM goes back to the roots of Rational Thermodynamics, particularly, to the Theory of Mixtures (TM), compare Truesdell & Toupin [30] and Bowen [31]. In contrast to the intuitive procedure proposed by Biot [21], the TPM provides each constituent of the porous medium with an individual motion function and an individual set of balance equations. Furthermore, in contrast to continuum-mechanics of single-phasic continua, the balance equations of the constituents of a multi-component aggregate are coupled to each other by the introduction of so-called production terms and can be summed up over all constituents to yield the standard set of balances of continuum mechanics. Following this, each component of the overall porous medium can be described separately, on the one hand, and is coupled to all the other components, on the other hand. For an extended review of the TPM, the interested reader may refer to de Boer [27] and Ehlers [29].

Treating porous media systems, it is easily concluded that coupled solid–fluid problems ask for a specific consideration other than traditional approaches. For example, Darcy's law, as one of the best known and simplest equations in this field, describes the motion of a flow through porous media. This empirical equation is widely adopted in engineering as a prescribed constitutive equation. Nevertheless, it is only valid under certain circumstances. Proceeding from the modern approach of the TPM, one recognises from the exploitation of the entropy inequality of the overall porous medium, which yields among other results also a constitutive relation for the fluid momentum production, and the momentum balance of the pore fluid that Darcy's law is not a constitutive equation but a result that only holds in the absence of acceleration terms and vanishing frictional pore-fluid stresses. The reader who is interested in various applications of the TPM is referred, for example, to Ehlers & Markert [32], Ehlers [33], Karajan [34] or Rempler [35] and many others.

Scientific articles tackling fracking porous media date back, for example, to Boone & Ingraffea [36], Boone & Detournay [37] or Detournay [38], who developed on the basis of Biot's theory a theoretical approach obtained under certain assumptions, such as the distribution of the pore pressure in the crack zone. In limited situations, these assumptions may be satisfied and analytical solutions can be derived. However, in more general cases, analytical solutions are not derivable anymore. Mikelić et al. [39,40] combined the Biot theory with the phase-field model to trigger the propagation of a fluid-pressurised crack in a poroelastic environment. Recently, Miehe & Mauthe [41] applied the phase-field modelling of fracture to the prediction of fluid- and moisture-driven crack propagation in deforming porous media based on Biot's poroelastic model, while Miehe et al. [42] set an additional threshold for the crack evolution and related the crack propagation only to the effective-tensile-stress-induced energy. However, unlike the TPM, Biot's theory does not involve the balance equations of each constituent including production terms like it is done in the TPM. As a result, the constitutive behaviour of the solid and the pore fluid is somehow ad hoc, meaning that it is not based on thermodynamic principles, which makes it difficult to individually describe the motion of the pore fluid and the porous solid skeleton. As a result, a transfer from Darcy-type flow to Navier–Stokes-type flow is

awkward to be realised within the evolving crack zone. Instead of this transfer, a higher permeability is prescribed in the crack zone, such that the fluid is observed to flow much faster.

Apart of a recent proceedings article of Markert & Heider [43], the present article firstly combines the concepts of the TPM and the phase-field model for the description of fracture in saturated porous media. By use of this concept, it is easy to extend the solid behaviour by phase-field variables and to couple this model to pore-fluid flow.

The present article is organised as follows. After shortly introducing the basic concepts, such as motion, volume fraction, and effective and partial density, the kinematics and the spectral decomposition of the solid strain are introduced on the basis of a small-strain approach followed by the balance equations of the constituents and the *Clausius–Planck* inequality of the overall aggregate. Thereafter, the constitutive equations of the model together with the evolution equation of the phase-field variable are introduced, where their thermodynamic consistency is additionally shown. Based on this model, some benchmark examples are performed, where fracturing processes of single- and multiphasic material are realised.

2. A brief introduction to fracturing porous media with pore content

The following description of fracturing porous media proceeds from an elastic porous solid saturated with a single pore fluid such as water. This aggregate is described on the macroscopic scale by use of the TPM, compare, for example, Ehlers [29], while the TPM itself combines the Theory of Mixtures (TM) with the concept of volume fractions, compare, for example, Bowen [24,31]. As a result, the TPM makes use of a homogenisation of the solid's microstructure by smearing out the solid and the pore fluid over the whole domain, such that one obtains superimposed continua with internal interactions driven by production terms.

Smearing out local microstructures towards a mean-field theory yields a loss of microstructural information of the individual components, which, in case of cracking solids can be re-introduced by means of a so-called length-scale parameter. Furthermore, since both components, solid and pore fluid, depend on their own constitutive variables on the microscale and considering that a homogenisation procedure does not gain information, use is made of the principle of phase separation (Ehlers [44]). This principle states that the free energy of an individual component of the overall aggregate, as on the microscale, does only depend on its own constitutive variables.

2.1. The concept of volume fractions

Restricting the porous medium under consideration to two components, solid and pore fluid, the overall aggregate φ is composed of the porous solid skeleton φ^S and the pore fluid φ^F, viz.:

$$\varphi = \bigcup_\alpha \varphi^\alpha = \varphi^S \bigcup \varphi^F. \tag{1}$$

The local volume element $\mathrm{d}v$ of φ, also called bulk volume element, is composed of the local volumes $\mathrm{d}v^S$ and $\mathrm{d}v^F$ of the components φ^S and φ^F. Volume fractions are defined via

$$n^\alpha := \frac{\mathrm{d}v^\alpha}{\mathrm{d}v} \quad \text{with} \quad \alpha = \{S, F\}, \quad \text{such that} \quad n^S + n^F = 1, \tag{2}$$

where $(2)_2$ represents the so-called saturation condition. Based on (2), one introduces two different density functions for each component, namely the real or effective density $\rho^{\alpha R}$ and the partial or bulk density ρ^α given by

$$\rho^{\alpha R} := \frac{\mathrm{d}m^\alpha}{\mathrm{d}v^\alpha} \quad \text{and} \quad \rho^\alpha := \frac{\mathrm{d}m^\alpha}{\mathrm{d}v}. \tag{3}$$

While the effective density relates the local mass element $\mathrm{d}m^\alpha$ to the volume element $\mathrm{d}v^\alpha$ of φ^α, the partial density relates $\mathrm{d}m^\alpha$ to the bulk volume element $\mathrm{d}v$. Obviously, the density functions are related to each other by

$$\rho^\alpha = n^\alpha \rho^{\alpha R}. \tag{4}$$

The density of the overall aggregate, also called mixture density, is defined as the sum of the partial densities of the constituents:

$$\rho := \sum_{\alpha} \frac{\mathrm{d}m^{\alpha}}{\mathrm{d}v} = \sum_{\alpha} n^{\alpha} \rho^{\alpha R}. \tag{5}$$

In a solid–liquid aggregate, one usually assumes both constituents to be materially incompressible. While $\rho^{FR} = const.$ at constant temperature is a standard assumption in hydraulics, the assumption of a materially incompressible porous solid is based on the fact that changes in the effective solid density are negligible in comparison with variations of the solid bulk density. As a result,

$$\rho^{\alpha R} = const. \tag{6}$$

as far as no temperature variations come into play. In this case, the bulk densities can only vary through variations of the volume fractions.

2.2. Kinematic setting and spectral decomposition of strains

In a multicomponent aggregate with superimposed constituents, an individual motion function is assigned to each constituent as

$$\mathbf{x} = \boldsymbol{\chi}_{\alpha}(\mathbf{X}_{\alpha}, t), \tag{7}$$

where $\mathbf{x}$ is the current position of superimposed material points of φ^{α} at time t with referential positions $\mathbf{X}_{\alpha}$ at time t_0. In a *Lagrange*an setting, the velocity and acceleration functions of φ^{α} are defined as

$$\mathbf{x}'_{\alpha} = \mathbf{v}_{\alpha} := \frac{\mathrm{d}}{\mathrm{d}t} \boldsymbol{\chi}_{\alpha}(\mathbf{X}_{\alpha}, t) \quad \text{and} \quad \mathbf{x}''_{\alpha} = (\mathbf{v}_{\alpha})'_{\alpha} := \frac{\mathrm{d}^2}{\mathrm{d}t^2} \boldsymbol{\chi}_{\alpha}(\mathbf{X}_{\alpha}, t) \tag{8}$$

and can be turned into an *Euler*ian setting by

$$\mathbf{x}'_{\alpha} = \mathbf{v}_{\alpha}(\mathbf{x}, t) \quad \text{and} \quad \mathbf{x}''_{\alpha} = (\mathbf{v}_{\alpha})'_{\alpha} = \mathbf{a}_{\alpha}(\mathbf{x}, t). \tag{9}$$

The kinematic description of a saturated porous solid is based on a *Lagrange*an description of the solid material by use of the displacement vector $\mathbf{u}_S := \mathbf{x} - \mathbf{X}_S$ and a modified *Euler*ian description of the pore fluid based on the seepage velocity $\mathbf{w}_F := \mathbf{v}_F - \mathbf{v}_S$ describing the fluid motion relative to the solid deformation.

Based on individual velocities of the components φ^{α}, one has to distinguish between individual material time derivatives. For an arbitrary scalar quantity $(\cdot)$, the material time derivative reads

$$(\cdot)'_{\alpha} = \frac{\mathrm{d}_{\alpha}(\cdot)}{\mathrm{d}t} = \frac{\partial(\cdot)}{\partial t} + \mathrm{grad}\,(\cdot)\,\mathbf{v}_{\alpha}. \tag{10}$$

Furthermore, the spatial and material gradient of $(\cdot)$, the latter only with respect to the motion of solid skeleton, are given by

$$\mathrm{grad}\,(\cdot) := \frac{\partial(\cdot)}{\partial \mathbf{x}} \quad \text{and} \quad \mathrm{Grad}_S\,(\cdot) := \frac{\partial(\cdot)}{\partial \mathbf{X}_S}. \tag{11}$$

If the solid material is described in a geometrically linear setting, the difference between the spatial and the referential gradient is negligible, such that $\mathrm{Grad}_S\,(\cdot) \approx \mathrm{grad}\,(\cdot)$. Consequently, the same is true for the corresponding divergence operators $\mathrm{Div}_S\,(\cdot) \approx \mathrm{div}\,(\cdot)$.

By use of a geometrically linear description of the porous solid material, the solid strain $\boldsymbol{\varepsilon}_S$ is expressed as the linearised version of the *Green–Lagrange*an strain $\mathbf{E}_S$. Thus, the linear strain and its temporal derivative $(\boldsymbol{\varepsilon}_S)'_{\alpha}$ are given by

$$\mathrm{lin.}\,\mathbf{E}_S = \boldsymbol{\varepsilon}_S := \frac{1}{2}(\mathrm{grad}\,\mathbf{u}_S + \mathrm{grad}^T\mathbf{u}_S) \quad \text{and} \quad (\boldsymbol{\varepsilon}_S)'_S = \frac{1}{2}(\mathrm{grad}\,\mathbf{v}_S + \mathrm{grad}^T\mathbf{v}_S). \tag{12}$$

Note in passing that $(\boldsymbol{\varepsilon}_S)'_S \approx \mathbf{D}_S$ and

$$\mathbf{D}_F := \frac{1}{2}(\operatorname{grad} \mathbf{v}_F + \operatorname{grad}^T \mathbf{v}_F), \tag{13}$$

where $\mathbf{D}_\alpha$ defines the rate of deformation tensor.

As $\boldsymbol{\varepsilon}_S$ is a symmetric tensor with real eigenvalues λ_{Si}, a spectral decomposition yields

$$\boldsymbol{\varepsilon}_S = \sum_i \lambda_{Si} \, \mathbf{n}_{Si} \otimes \mathbf{n}_{Si}, \tag{14}$$

where $\mathbf{n}_{Si}$ are the eigenvectors corresponding to λ_{Si}. Based on (14), $\boldsymbol{\varepsilon}_S$ can be split into a positive and a negative part via

$$\boldsymbol{\varepsilon}_S^+ = \sum_i \frac{\lambda_{Si} + |\lambda_{Si}|}{2} \, \mathbf{n}_{Si} \otimes \mathbf{n}_{Si} \quad \text{and} \quad \boldsymbol{\varepsilon}_S^- = \sum_i \frac{\lambda_{Si} - |\lambda_{Si}|}{2} \, \mathbf{n}_{Si} \otimes \mathbf{n}_{Si}, \tag{15}$$

where $\boldsymbol{\varepsilon}_S^+$ only contains positive and $\boldsymbol{\varepsilon}_S^-$ only negative eigenvalues. Obviously, $\boldsymbol{\varepsilon}_S = \boldsymbol{\varepsilon}_S^+ + \boldsymbol{\varepsilon}_S^-$.

2.3. Governing balance equations and Clausius–Planck inequality

Describing a fluid-saturated porous solid in an isothermal environment, the governing equations of the TPM are given by the mass and momentum balances, viz.:

$$\begin{aligned} \text{mass:} \quad & (\rho^\alpha)'_\alpha + \rho^\alpha \operatorname{div} \mathbf{\overset{'}{x}}_\alpha = \hat{\rho}^\alpha, \\ \text{momentum :} \quad & \rho^\alpha \mathbf{\overset{''}{x}}_\alpha = \operatorname{div} \mathbf{T}^\alpha + \rho^\alpha \mathbf{g} + \hat{\mathbf{p}}^\alpha. \end{aligned} \tag{16}$$

Therein, $\hat{\rho}^\alpha$ and $\hat{\mathbf{p}}^\alpha$ are the density and the direct momentum production terms of constituent φ^α, $\mathbf{T}^\alpha$ defines the *Cauchy* stresses of φ^α, and $\mathbf{g}$ is the gravitation vector. To ensure that the constitutive equations for the stresses and the production terms are thermodynamically admissible, they have to fulfil the entropy inequality, which, in case of isothermal processes, can be given in terms of the *Clausius–Planck* inequality

$$\sum_\alpha \left[\mathbf{T}^\alpha \cdot \mathbf{D}_\alpha - \rho^\alpha (\psi^\alpha)'_\alpha - \hat{\mathbf{p}}^\alpha \cdot \mathbf{\overset{'}{x}}_\alpha \right] \geqq 0, \tag{17}$$

where ψ^α is the *Helmholtz* free energy of φ^α per mass element. For details on the derivative of the complete set of thermodynamical balances of porous-media aggregates and mixtures, the reader is referred, for example, to Ehlers [29].

Since there is no mass transfer between a pore fluid, such as water, and a solid skeleton, such as rock or soil, the mass production terms vanish. As a result, the direct momentum productions are constrained by

$$\hat{\mathbf{p}}^S + \hat{\mathbf{p}}^F = \mathbf{0}. \tag{18}$$

Furthermore, by use of the incompressibility constraints of solid and fluid yielding $\rho^{\alpha R} = const.$, the mass balance equations can be expressed as volume balances:

$$(n^\alpha)'_\alpha + n^\alpha \operatorname{div} \mathbf{\overset{'}{x}}_\alpha = 0. \tag{19}$$

Combining this equation with the saturation condition $(2)_2$, one obtains the incompressibility constraint of the overall aggregate:

$$n^S \operatorname{div} \mathbf{v}_S + n^F \operatorname{div} \mathbf{v}_F + \operatorname{grad} n^F \cdot \mathbf{w}_F = 0. \tag{20}$$

After multiplication with a *Lagrange* multiplier p and addition to the inequality (17), one obtains the *Clausius–Planck* inequality in its final form with p as the pore pressure:

$$\left(\mathbf{T}^S + n^S p\mathbf{I} \right) \cdot \mathbf{D}_S - \rho^S (\psi^S)'_S + \left(\mathbf{T}^F + n^F p\mathbf{I} \right) \cdot \mathbf{D}_F - \rho^F (\psi^F)'_F - \left(\hat{\mathbf{p}}^F - p \operatorname{grad} n^F \right) \cdot \mathbf{w}_F \geqq 0. \tag{21}$$

Given this inequality, one recovers the terms in parentheses as the extra solid and fluid stresses and the extra fluid momentum production, viz.:

$$\mathbf{T}_E^S := \mathbf{T}^S + n^S\, p\mathbf{I}, \quad \mathbf{T}_E^F := \mathbf{T}^F + n^F\, p\mathbf{I}, \quad \hat{\mathbf{p}}_E^F := \hat{\mathbf{p}}^F - p\,\mathrm{grad}\, n^F. \tag{22}$$

2.4. Constitutive setting of solid skeleton and pore fluid

Based on the fact that solid and pore fluid are joint together in the TPM by means of a real or a virtual homogenisation over the microstructure of the porous solid, the principle of phase or constituent separation comes into play (Ehlers [44]) stating that the free energy of each constituent only depends on constitutive variables of the component under consideration and not, as in the constitutive description of real mixtures, of all variables involved. As a result and under consideration of an isothermal setting with materially incompressible constituents, the solid free energy basically depends on the deformation gradient, while the fluid free energy is constant, viz.:

$$\psi^S = \psi^S(\mathbf{F}_S), \quad \psi^F = \psi^F(-). \tag{23}$$

While the dependency of ψ^S on $\mathbf{F}_S$ can usually be reduced to the right *Cauchy–Green* deformation tensor $\mathbf{C}_S$ or the *Green–Lagrange*an strain $\mathbf{E}_S$, the consideration of fracturing porous media induces further constitutive information, which, by use of a phase-field approach, is given by an order parameter ϕ^S, the phase field, and its solid-material gradient $\mathrm{Grad}_S\,\phi^S$:

$$\psi^S = \psi^S(\mathbf{E}_S,\ \phi^S,\ \mathrm{Grad}_S\,\phi^S) \approx \psi^S(\boldsymbol{\varepsilon}_S,\ \phi^S,\ \mathrm{grad}\,\phi^S). \tag{24}$$

Note in passing that the right-hand side of this relation corresponds to the small-strain approach of the porous solid, where $\mathbf{E}_S \approx \boldsymbol{\varepsilon}_S$ and $\mathrm{Grad}_S(\cdot) \approx \mathrm{grad}\,(\cdot)$.

The order parameter or phase field ϕ^S with $0 \leq \phi^S \leq 1$ can also be interpreted as damage variable d of damage mechanics and is used for the detection and the description of broken or cracked zones in the solid. ϕ^S has the bounding properties

$$\phi^S = \begin{cases} 0 & \text{for intact material,} \\ 1 & \text{for fully cracked material.} \end{cases} \tag{25}$$

As far as the solid is not fractured (intact), ϕ^S and, as result, $\mathrm{grad}\,\phi^S$ vanish and ψ^S reduces to the standard stored elastic energy $\psi^S(\boldsymbol{\varepsilon}_S)$. However, taking the solid time derivative of $\psi^S(\boldsymbol{\varepsilon}_S,\ \phi^S,\ \mathrm{grad}\,\phi^S)$ yields

$$(\psi^S)_S' = \frac{\partial \psi^S}{\partial \boldsymbol{\varepsilon}_S} \cdot (\boldsymbol{\varepsilon}_S)_S' + \frac{\partial \psi^S}{\partial \phi^S}(\phi^S)_S' + \frac{\partial \psi^S}{\partial\, \mathrm{grad}\,\phi^S} \cdot \mathrm{grad}\,(\phi^S)_S'. \tag{26}$$

For the application of (26) to the entropy inequality (21), it is advantageous to multiply the whole equation with the partial solid density $\rho_0^S = (\det \mathbf{F}_S)\,\rho^S$ of the solid reference configuration at time t_0. Then, a transformation of the last term of (26) yields with the aid of the divergence theorem

$$\rho_0^S \frac{\partial \psi^S}{\partial\, \mathrm{grad}\,\phi^S} \cdot \mathrm{grad}\,(\phi^S)_S' = \mathrm{div}\left[(\phi^S)_S'\,\rho_0^S\,\frac{\partial \psi^S}{\partial\, \mathrm{grad}\,\phi^S}\right] - (\phi^S)_S'\,\mathrm{div}\left(\rho_0^S\,\frac{\partial \psi^S}{\partial\, \mathrm{grad}\,\phi^S}\right). \tag{27}$$

Combining this result with the *Clausius–Planck* inequality (21), and the extra terms (22) and (23)$_2$ results in

$$(\det \mathbf{F}_S)^{-1}\left(\boldsymbol{\sigma}_E^S - \rho_0^S\,\frac{\partial \psi^S}{\partial \boldsymbol{\varepsilon}_S}\right) \cdot (\boldsymbol{\varepsilon}_S)_S' - (\det \mathbf{F}_S)^{-1}\left[\rho_0^S\,\frac{\partial \psi^S}{\partial \phi^S} - \mathrm{div}\left(\rho_0^S\,\frac{\partial \psi^S}{\partial\, \mathrm{grad}\,\phi^S}\right)\right](\phi^S)_S'$$

$$- (\det \mathbf{F}_S)^{-1}\mathrm{div}\left((\phi^S)_S'\,\rho_0^S\,\frac{\partial \psi^S}{\partial\, \mathrm{grad}\,\phi^S}\right) + \mathbf{T}_E^F \cdot \mathbf{D}_F - \hat{\mathbf{p}}_E^F \cdot \mathbf{w}_F \geqq 0. \tag{28}$$

In (28), $\boldsymbol{\sigma}_E^S$ is the linearised solid extra stress corresponding to the second *Piola–Kirchhoff* stress $\mathbf{S}_E^S = (\det \mathbf{F}_S) \mathbf{F}_S^{-1} \mathbf{T}_E^S \mathbf{F}_S^{T-1}$. Multiplying this inequality by $\det \mathbf{F}_S > 0$, an exploitation of (28) yields

$$\boldsymbol{\sigma}_E^S = \rho_0^S \frac{\partial \psi^S}{\partial \boldsymbol{\varepsilon}_S}, \quad \mathrm{div}\left((\phi^S)'_S \rho_0^S \frac{\partial \psi^S}{\partial \, \mathrm{grad}\, \phi^S}\right) = 0 \tag{29}$$

and the dissipation inequality

$$-\left[\rho_0^S \frac{\partial \psi^S}{\partial \phi^S} - \mathrm{div}\left(\rho_0^S \frac{\partial \psi^S}{\partial \, \mathrm{grad}\, \phi^S}\right)\right](\phi^S)'_S + \det \mathbf{F}_S \left(\mathbf{T}_E^F \cdot \mathbf{D}_F - \hat{\mathbf{p}}_E^F \cdot \mathbf{w}_F\right) \geqq 0. \tag{30}$$

To fulfil the dissipation inequality, one has to introduce an evolution equation for the order parameter ϕ^S and sufficient conditions for $\mathbf{T}_E^F$ and $\hat{\mathbf{p}}_E^F$, viz.:

$$\begin{aligned} (\phi^S)'_S &\propto -\left[\rho_0^S \frac{\partial \psi^S}{\partial \phi^S} - \mathrm{div}\left(\rho_0^S \frac{\partial \psi^S}{\partial \, \mathrm{grad}\, \phi^S}\right)\right], \\ \mathbf{T}_E^F &\propto \mathbf{D}_F, \\ \hat{\mathbf{p}}_E^F &\propto -\mathbf{w}_F. \end{aligned} \tag{31}$$

Given (29) and (31), (29)$_1$ is fairly standard in small-strain porous media elasticity, while (29)$_2$ describes the continuity of the vectorial term in parentheses, like the continuity equation of fluid mechanics, $\mathrm{div}\,\mathbf{v} = 0$, describes the continuity of the velocity field $\mathbf{v}$ of a single incompressible fluid.

Given this interpretation, integration of (29)$_2$ over a volumetric domain Ω combined with the use of the *Gauss*ian integral theorem relating volume to surface integrals and vice versa yields

$$\int_\Omega \mathrm{div}\left((\phi^S)'_S \rho_0^S \frac{\partial \psi^S}{\partial \, \mathrm{grad}\, \phi^S}\right) \mathrm{d}v = \int_{\partial\Omega} \left((\phi^S)'_S \rho_0^S \frac{\partial \psi^S}{\partial \, \mathrm{grad}\, \phi^S}\right) \cdot \mathbf{n}\, \mathrm{d}a = 0, \tag{32}$$

where Ω is an arbitrary volume and $\partial\Omega$ its surface with outward-oriented unit surface normal $\mathbf{n}$. In a numerical implementation, (32) can be realised by the introduction of the following boundary condition:

$$\frac{\partial \psi^S}{\partial \, \mathrm{grad}\, \phi^S} \cdot \mathbf{n} = 0. \tag{33}$$

The non-equilibrium conditions (31) can be satisfied by

$$\begin{aligned} (\phi^S)'_S &= -\frac{1}{M}\left[\rho_0^S \frac{\partial \psi^S}{\partial \phi^S} - \mathrm{div}\left(\rho_0^S \frac{\partial \psi^S}{\partial \, \mathrm{grad}\, \phi^S}\right)\right], \\ \mathbf{T}_E^F &= 2(\phi^S)^2 n^F \mu^{FR} \mathbf{D}_F, \\ \hat{\mathbf{p}}_E^F &= -(1 - \phi^S)^2 \frac{(n^F)^2 \gamma^{FR}}{k^F} \mathbf{w}_F. \end{aligned} \tag{34}$$

Therein, $M > 0$ is introduced as the mobility parameter, while μ^{FR} is the effective dynamic viscosity of the pore fluid, $\gamma^{FR} = \rho^{FR} g$ with $g = |\mathbf{g}|$ its specific weight, and k^F the hydraulic conductivity, which is related to the intrinsic permeability K^S of the solid via

$$k^F = \frac{\gamma^{FR}}{\mu^{FR}} K^S. \tag{35}$$

The combination of the order parameter ϕ^S with the dynamic viscosity μ^{FR} in (34)$_2$ yields the viscous extra stress $\mathbf{T}_E^F$ to vanish in the intact porous domain but to occur in the cracked zone. At the same time, the extra momentum production $\hat{\mathbf{p}}_E^F$ or the effective drag force between solid and pore fluid, respectively, vanishes in the fully cracked zone but dominates the pore-fluid flow in the unbroken domain. This effect is in accordance with a dimensional analysis exhibiting that the friction force $\mathrm{div}\,\mathbf{T}_E^F$ incorporated in the momentum balance of φ^F can be neglected in comparison

with $\hat{\mathbf{p}}_E^F$ in case of a pure porous-media flow but is dominant in case of a *Stokes* flow in a bulk fluid with negligible drag, cf. Ehlers et al. [45].

Based on (34)$_1$, one notices that the evolution of ϕ^S only depends on the energetic changes of the porous solid. This is reasonable since cracks can only exist in the solid skeleton and not in the pore fluid. Furthermore, in a closed porous domain with a materially incompressible solid and a materially incompressible pore fluid with no possibility to flow in or out of the domain, an arbitrary pore pressure would not lead to solid deformations and also not to any kind of fracture. In this sense, hydraulic fracture is an indirect result of fluid pressure but a direct result of solid deformation. Thus, following basic papers on phase-field fracture for a pure solid-mechanical problem by Kuhn & Müller [15] and Miehe et al. [17], the solid *Helmholtz* free energy (24) is assumed as

$$\rho_0^S \psi^S(\boldsymbol{\varepsilon}_S, \phi^S, \operatorname{grad}\phi^S) = \left[(1-\phi^S)^2 + \eta_r^S\right]\rho_0^S \psi^{S+}(\boldsymbol{\varepsilon}_S^+) + \rho_0^S \psi^{S-}(\boldsymbol{\varepsilon}_S^-) + G_c\,\Gamma^S(\phi^S, \operatorname{grad}\phi^S), \tag{36}$$

where
$$
\begin{cases}
\rho_0^S \psi^{S+}(\boldsymbol{\varepsilon}_S^+) = \mu^S\,(\boldsymbol{\varepsilon}_S^+ \cdot \boldsymbol{\varepsilon}_S^+) + \dfrac{1}{2}\lambda^S\left(\dfrac{\operatorname{tr}\boldsymbol{\varepsilon}_S + |\operatorname{tr}\boldsymbol{\varepsilon}_S|}{2}\right)^2, \\[4mm]
\rho_0^S \psi^{S-}(\boldsymbol{\varepsilon}_S^-) = \mu^S\,(\boldsymbol{\varepsilon}_S^- \cdot \boldsymbol{\varepsilon}_S^-) + \dfrac{1}{2}\lambda^S\left(\dfrac{\operatorname{tr}\boldsymbol{\varepsilon}_S - |\operatorname{tr}\boldsymbol{\varepsilon}_S|}{2}\right)^2, \\[4mm]
\Gamma^S(\phi^S, \operatorname{grad}\phi^S) = \dfrac{1}{2\epsilon}(\phi^S)^2 + \dfrac{\epsilon}{2}\operatorname{grad}\phi^S \cdot \operatorname{grad}\phi^S.
\end{cases}
\tag{37}
$$

In (36), the total stress energy $\rho_0^S \psi^S$ per bulk volume is governed by three terms defining, firstly, the tensile energy, secondly, the compressive energy and, thirdly, the fracture energy including the critical energy release rate G_c of brittle fracture and the crack surface density function Γ^S depending on the phase-field variable, its gradient and the internal length-scale parameter ϵ responsible for the thickness of broken zones. The interested reader might consider Miehe et al. [46], where a study of a diffusive crack topology is included with the width transferred from wide to narrow with shrinking values of ϵ. Furthermore, the first term of (36) is governed by the factor $[(1-\phi^S)^2 + \eta_r^S]$. As a result, it vanishes in fully broken zones apart of a viscous stress resistance governed by η_r^S, while the compressive energy expressed by the second term of (36) is independent of the fact, whether the solid is broken or not. Finally, it should be noted that the fracture energy mainly governs the evolution of the order parameter ϕ^S.

Given (36) and (37), the linearised effective stress tensor of the solid skeleton is obtained with the aid of (29)$_1$ yielding

$$
\begin{aligned}
\boldsymbol{\sigma}_E^S &= \rho_0^S \frac{\partial \psi^S}{\partial \boldsymbol{\varepsilon}_S} \\
&= \left[(1-\phi^S)^2 + \eta_r^S\right]\left[2\,\mu^S\,\boldsymbol{\varepsilon}_S^+ + \lambda^S\left(\frac{\operatorname{tr}\boldsymbol{\varepsilon}_S + |\operatorname{tr}\boldsymbol{\varepsilon}_S|}{2}\right)\mathbf{I}\right] + 2\,\mu^S\,\boldsymbol{\varepsilon}_S^- + \lambda^S\left(\frac{\operatorname{tr}\boldsymbol{\varepsilon}_S - |\operatorname{tr}\boldsymbol{\varepsilon}_S|}{2}\right)\mathbf{I}.
\end{aligned}
\tag{38}
$$

Furthermore, (34)$_1$, (36) and (37) combine to the evolution equation of ϕ^S yielding

$$(\phi^S)_S' = \frac{1}{M}\left[2(1-\phi^S)\,\rho_0^S\psi^{S+} - G_c\left(\frac{\phi^S}{\epsilon} - \epsilon\,\operatorname{div}\operatorname{grad}\phi^S\right)\right], \tag{39}$$

where (33) additionally induces the boundary condition

$$G_c\,\epsilon\,\operatorname{grad}\phi^S \cdot \mathbf{n} = 0. \tag{40}$$

2.5. Fracturing as an irreversible process

Geomaterials, such as shale, are incapable of self-healing. Once a crack occurs in the material, this change is maintained and the loss of resistance in the cracked zone is not recoverable. By use of the phase-field theory, the cracking zone is marked by the order parameter ϕ^S with $\phi^S = 1$ in the fully cracked state. The evolution of ϕ^S from 0 of the

Table 1
Summary of governing partial differential equations.

Solid displacement–velocity relation:
$$(\mathbf{u}_S)'_S = \mathbf{v}_S$$
Overall volume balance:
$$\operatorname{div}\left(\mathbf{v}_S + n^F \mathbf{w}_F\right) = 0$$
Solid momentum balance:
$$\rho^S(\mathbf{v}_S)'_S = \operatorname{div}\boldsymbol{\sigma}^S_E - n^S \operatorname{grad} p + \rho^S \mathbf{g} - \hat{\mathbf{p}}^F_E$$
Fluid momentum balance:
$$\rho^F(\mathbf{v}_F)'_F = \operatorname{div}\mathbf{T}^F_E - n^F \operatorname{grad} p + \rho^F \mathbf{g} + \hat{\mathbf{p}}^F_E$$
Phase-field evolution equation:
$$(\phi^S)'_S = \frac{1}{M}\left[2(1-\phi^S)\mathcal{H} - \frac{G_c}{\epsilon}(\phi^S - \epsilon^2 \operatorname{div}\operatorname{grad}\phi^S)\right]$$

intact state towards 1 is governed by the accumulation of micro cracks. Consequently, it must fulfil the restriction

$$(\phi^S)'_S \geqq 0. \tag{41}$$

Based on the evolution (39), the irreversibility of the fracturing process is defined by

$$(\phi^S)'_S = \operatorname{Max}\left\{\frac{1}{M}\left[2(1-\phi^S)\,\rho_0^S \psi^{S+} - G_c\left(\frac{\phi^S}{\epsilon} - \epsilon \operatorname{div}\operatorname{grad}\phi^S\right)\right], 0\right\}. \tag{42}$$

For the numerical implementation, a history variable of the form

$$\mathcal{H} = \operatorname*{Max}_{t \geqq t_0}(\rho_0^S \psi^{S+}) \tag{43}$$

is introduced, such that the evolution equation reads

$$(\phi^S)'_S = \frac{1}{M}\left[2(1-\phi^S)\,\mathcal{H} - G_c\left(\frac{\phi^S}{\epsilon} - \epsilon \operatorname{div}\operatorname{grad}\phi^S\right)\right]. \tag{44}$$

Note that the consideration of the history variable $\mathcal{H}$ based on the so-called pseudo-elastic potential $\rho_0^S \psi^{S+}$ has firstly been introduced to phase-field-driven fracture by Miehe et al. [17].

Combining Eq. (16)$_2$, (18) and (20) yields the governing set of balance relations given in Table 1 corresponding to the primary variables of the problem. In particular, the overall volume balance corresponds to the pore pressure p, while the solid momentum balance corresponds to the solid displacement $\mathbf{u}_S$ and the fluid momentum balance to the pore-fluid velocity $\mathbf{v}_F$. For the reduction of the solid momentum balance from second order to first order in time, the solid displacement–velocity relation is included and corresponds to the determination of the solid velocity $\mathbf{v}_S$. In addition to these equations, which are sufficient for the handling of standard dynamical problems of saturated porous media, the phase-field evolution equation is included in the set of Table 1 and corresponds to the phase-field variable ϕ^S. The phase-field evolution equation, which is based on a history variable $\mathcal{H}$, plays a role in the fracture-evolution problem comparable to the role of the evolution of plastic strains in plasticity. Like the plastic strains in plasticity, one could compute the phase field ϕ^S at the *Gauss*-point level during the finite-element analysis (FEA) to gain the same result as here, where the computation of ϕ^S is included in the overall computation procedure as one of the governing equations of the FEA. Note in passing that the same procedure as is used here can also successfully be applied in elasto-plasticity, cf. Rempler et al. [47].

3. Numerical treatment

Together with initial and boundary conditions, the equations of Table 1 exhibit the strong form of the initial–boundary-value problem. Multiplication of these equations with the test functions $\delta\mathbf{v}_S$, δp, $\delta\mathbf{u}_S$, $\delta\mathbf{v}_F$ and $\delta\phi^S$ yields the weak form of the governing partial differential equations, cf. Table 2. To obtain these equations, the relations of Table 1 have been multiplied with their test functions and have been integrated over the *Lagrange*an domain $\mathcal{B}$. Finally, integration by parts and the application of the *Gauss*ian integral theorem yield the displayed results, where

Table 2

Weak form of the governing partial differential equations.

Solid displacement–velocity relation:

$$\mathcal{G}_{\mathbf{v}_S} = \int_{\mathcal{B}} [\,(\mathbf{u}_S)'_S - \mathbf{v}_S\,] \cdot \delta\mathbf{v}_S \, dv = 0$$

Overall volume balance:

$$\mathcal{G}_p = \int_{\mathcal{B}} \left(\operatorname{div}\mathbf{v}_S\,\delta p - n^F \mathbf{w}_F \cdot \operatorname{grad}\delta p \right) dv + \int_{\mathcal{S}} \bar{v}\,\delta p \, da = 0$$

Overall momentum balance:

$$\mathcal{G}_{\mathbf{u}_S} = \int_{\mathcal{B}} \Big[\left(\rho^S (\mathbf{v}_S)'_S + \rho^F [\,(\mathbf{v}_F)'_S + (\operatorname{grad}\mathbf{v}_F)\,\mathbf{w}_F\,] \right) \cdot \delta\mathbf{u}_S + (\boldsymbol{\sigma}^S_E + \mathbf{T}^F_E - p\,\mathbf{I}) \cdot \operatorname{grad}\delta\mathbf{u}_S$$
$$- (\rho^S + \rho^F)\,\mathbf{g} \cdot \delta\mathbf{u}_S \Big]\, dv - \int_{\mathcal{S}} \bar{\mathbf{t}} \cdot \delta\mathbf{u}_S\, da = 0$$

Fluid momentum balance:

$$\mathcal{G}_{\mathbf{v}_F} = \int_{\mathcal{B}} \Big(\rho^{FR}[\,(\mathbf{v}_F)'_S + (\operatorname{grad}\mathbf{v}_F)\,\mathbf{w}_F\,] \cdot \delta\mathbf{v}_F + (\mathbf{T}^{FR}_E - p\,\mathbf{I}) \cdot \operatorname{grad}\delta\mathbf{v}_F$$
$$- \frac{1}{n^F}\,p\,\operatorname{grad} n^F \cdot \delta\mathbf{v}_F - \rho^{FR}\mathbf{g} \cdot \delta\mathbf{v}_F - \hat{\mathbf{p}}^{FR}_E \cdot \delta\mathbf{v}_F \Big)\, dv - \int_{\mathcal{S}} \bar{\mathbf{t}}^{FR} \cdot \delta\mathbf{v}_F\, da = 0$$

Phase-field evolution equation:

$$\mathcal{G}_{\phi^S} = \int_{\mathcal{B}_S} \left([M(\phi^S)'_S - 2(1 - \phi^S)\mathcal{H} + \frac{G_c}{\epsilon}\phi^S]\,\delta\phi^S + G_c\epsilon\, \operatorname{grad}\phi^S \cdot \operatorname{grad}\delta\phi^S \right) dv$$
$$- \int_{\mathcal{S}} G_c\epsilon\, \operatorname{grad}\phi^S \cdot \mathbf{n}\,\delta\phi^S\, da = 0$$

the boundary terms are indicated by an additional bar. For a convenient computation of dynamic hydraulic fracturing problems, the momentum balances of solid and fluid have been added, yielding the boundary term $\bar{\mathbf{t}}$ to exhibit the complete load of the saturated porous solid. By this approach, the components of the model, solid and fluid, carry as much of the external load as corresponds to their states of deformation and motion. Furthermore, the pore-fluid equation is given with respect to the motion of the solid skeleton as a result of the modified *Euler*ian description. In addition, the equation of the fluid momentum balance has been divided by n^F, thus yielding the effective forms of fluid density, extra stress, extra momentum production and boundary term. In conclusion, the boundary and extra terms included in Table 2 read:

$$
\begin{aligned}
\mathbf{T}^{FR} &:= \frac{1}{n^F}\,(\mathbf{T}^F_E - n^F p\,\mathbf{I}), \\
\mathbf{T}^{FR}_E &:= \frac{1}{n^F}\,\mathbf{T}^F_E = 2(\phi^S)^2 \mu^{FR}\mathbf{D}_F, \\
\hat{\mathbf{p}}^{FR}_E &:= \frac{1}{n^F}\,\hat{\mathbf{p}}^F_E = -(1-\phi^S)^2 \frac{n^F \gamma^{FR}}{k^F}\,\mathbf{w}_F, \\
\bar{v} &:= n^F \mathbf{w}_F \cdot \mathbf{n}, \\
\bar{\mathbf{t}} &:= (\boldsymbol{\sigma}^S_E + \mathbf{T}^F_E)\,\mathbf{n} - p\,\mathbf{n}, \\
\bar{\mathbf{t}}^{FR} &:= \mathbf{T}^{FR}\mathbf{n} = \mathbf{T}^{FR}_E\mathbf{n} - p\,\mathbf{n}.
\end{aligned}
\tag{45}
$$

Furthermore, note that the solid extra stress $\boldsymbol{\sigma}^S_E$ is given by (38) and that the boundary term of the phase-field evolution equation vanishes with respect to (40). Finally, the FEA requires a discretisation of the overall problem in space and time. In order to satisfy standard stability requirements, such as the Ladyzhenskaya–Babuška–Brezzi (LBB) condition, the spatial discretisation of the fully coupled problem is based on *Taylor–Hood* elements with quadratic approximation functions for $\mathbf{u}_S$, $\mathbf{v}_S$ and $\mathbf{v}_F$ and linear approximation functions for the remainder of primary variables, compare Markert et al. [48]. Based on the reduction of the order of the overall momentum balance in time, the time discretisation proceeds from the backward *Euler* scheme within the implicit time-integration method. Based on the reduction of the order of the overall momentum balance in time, the time discretisation proceeds from the backward *Euler* scheme within the implicit time-integration method. The monolithic implicit scheme offers an unconditionally stable solution, compare Ehlers et al. [49]. Compared to the monolithic scheme, the computational efficiency gained by the partitioned strategy is not guaranteed for the case that differential equations are volumetrically coupled by production terms throughout the whole domain, compare Felippa & Park [50].
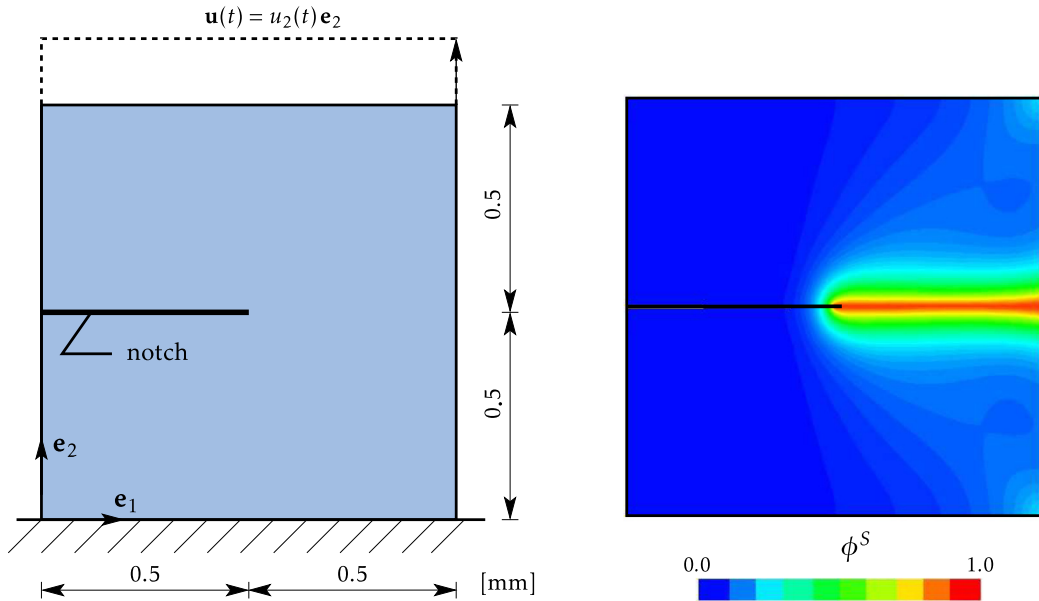
Fig. 1. Crack propagation in a single-phasic solid: (left) geometry and boundary conditions, (right) crack propagation displayed by the phase field ϕ^S.

Based on this procedure, it has been found that the spatial discretisation of the solid displacement-velocity relation yields some unexpected numerical inaccuracies, such that this relation is satisfied in its strong form at each *Gauss* point of the FEA, thus reducing the number of the nodal degrees of freedom (DOF). The following examples are computed by use of the numerical solver PANDAS,[1] which has been developed for the solution of strongly coupled problems based on partial differential equations (PDE).

4. Numerical examples

4.1. Verification for a single-phasic solid

The first example is used for the verification of the algorithm designed for the computation of dynamic problems of hydraulic fracturing. Here we proceed from the geometry and boundary conditions of the single-phasic solid that has been described in the literature as by Miehe et al. [17] and was later recalculated by Mikelić [39], cf. Fig. 1. In contrast to [17], the material parameters of Table 3 have been taken from the dissertation thesis of Hofacker [51]. However, in both cases, the inertial and gravitational forces have been neglected. This feature is also included in the present computation. Note in passing that this example does not demand the whole complexity of our algorithm, since here, we could disregard the pore content and could therefore proceed from linear approximation functions for $\mathbf{u}_S$. However, the coupling between the momentum balance and the phase-field evolution equation remained, while Hofacker proceeded from a decoupled solution scheme.

The displacement at the top edge is prescribed as $u_2(t) = 1 \times 10^{-5}t$ mm, and the loading is assumed to last for approx. 600 s such that a maximum displacement of approx. 0.006 mm is obtained. For the comparison of the present computation with the results of Hofacker [51], we proceed from 19,488 triangular elements with only one linear shape function for the solid displacement. The minimum mesh length of one element is about 5×10^{-3} mm and is applied in the expected crack area in continuation of the notch. As is shown in Fig. 1, a horizontal crack is proceeding through the material. Furthermore, the load–displacement curve for the top edge is presented in Fig. 2, where one can observe that the computed curve fits the referential result. Marginal differences between the present result and the result by Hofacker stem from the choice of different algorithms, which are chosen fully coupled (here) versus staggered (Hofacker) and from the fact that Hofacker did not publish the value of the viscous stress resistance η_r^S that she used in her calculations, such that we had to make a convenient guess.

---

[1] **P**orous media **A**daptive **N**onlinear finite-element solver based on **D**ifferential **A**lgebraic **S**ystems (http://www.get-pandas.com).

Table 3
Parameters for the single-phasic solid material.

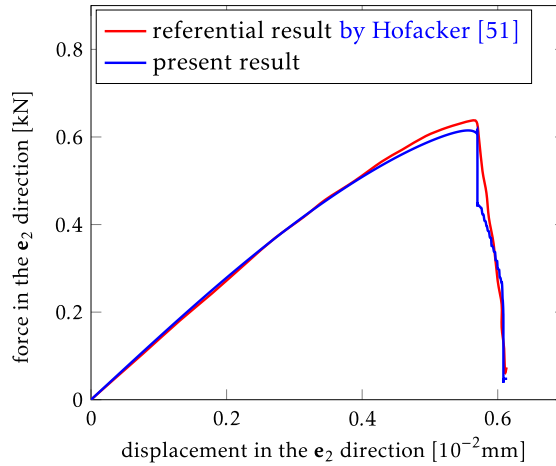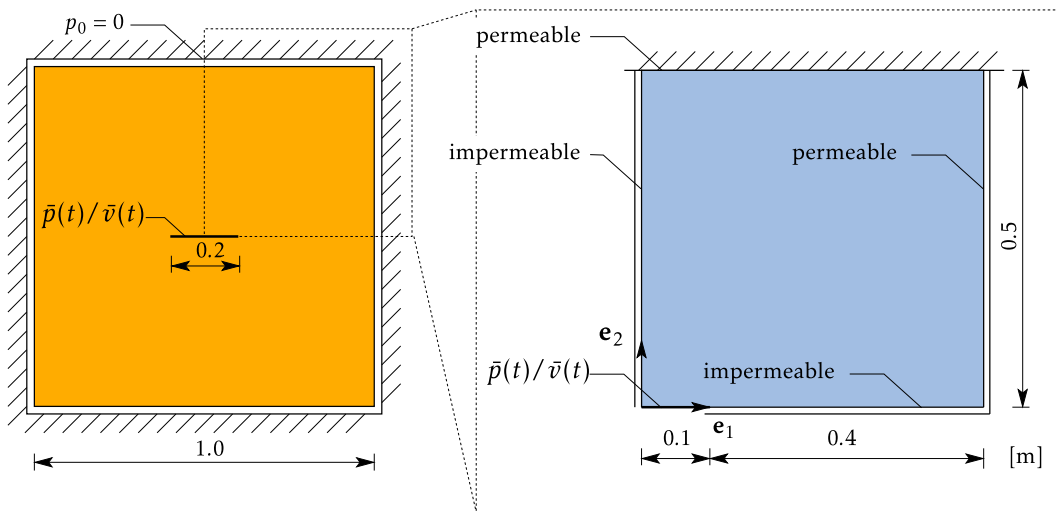| μ^S | 8.077×10^{10} Pa | λ^S | 12.115×10^{10} Pa | G_c | 2.7×10^3 N/m |
| ϵ | 3.75×10^{-3} m | η_r | 8×10^{-4} | M | 3×10^3 Ns/m² |

Fig. 2. Load–displacement curve of the top edge.

Fig. 3. Geometry and boundary conditions for the hydraulic fracturing problem.

4.2. Hydraulic fracturing in 2 dimensions

The second example simulates hydraulic fracturing of a fluid-saturated specimen under an increasing pore pressure or a fluid injection along the notch, cf. Fig. 3. Here, the main goal is to check the feasibility of modelling crack propagation in a pressure-driven load case. The geometry and boundary conditions are displayed in Fig. 3, while the material parameters can be taken from Table 4.

As a result of double symmetry, the computation is carried out for the top-right quarter, and the computational results can be complemented correspondingly. Within the FEA, this quarter is discretised by 792 quadrilateral *Taylor–Hood* elements with quadratic shape functions for $\mathbf{u}_S$ and $\mathbf{v}_F$ and linear shape functions for p and ϕ^S. The spatial discretisation results in a minimum element size of $h^e \approx 4 \times 10^{-3}$ m. Based on an investigation with linear quadrilateral elements by Hofacker [51] stating that to resolve the phase field in the numerical computation, the

Table 4
Parameters for the biphasic model.

μ^S	8.077×10^{10} Pa	λ^S	12.115×10^{10} Pa	G_c	2.7×10^3 N/m
ϵ	4×10^{-3} m	η_r	4×10^{-2}	M	3×10^3 Ns/m^2
μ^F	1.002×10^{-3} Pa/s	n_0^S	0.8	k^F	1×10^{-8} m/s
ρ_0^{SR}	3×10^3 kg/m^3	ρ^{FR}	1×10^3 kg/m^3		
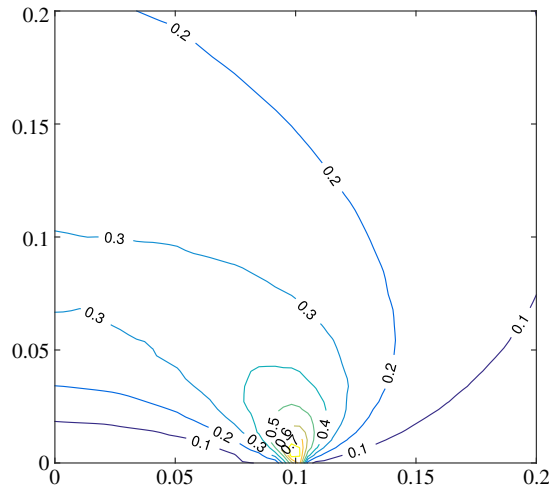
Fig. 4. Contours of scaled principal shear stresses τ^* at $t = 2331$ s in the vicinity of the notch.

length-scale parameter ϵ should not be smaller than $h^e/2$, ϵ has been chosen in this study to be in the same magnitude as h^e. However, additional studies will demonstrate the influence of ϵ on the evolution of the phase field. As the loading in the notch can be given by an increasing pore pressure or by a prescribed liquid influx, we will discuss both possibilities. In the first case, a uniform but increasing pressure of $\bar{p} = 5.5 \times 10^4\, t$ Pa is applied to the notch. This leads, for example, to contours of normalised principal shear stresses

$$\tau^* = \frac{\max \tau}{(\max \tau)^*} \tag{46}$$

as is seen in Fig. 4 for $t = 2331$ s, where $\max \tau$ is the largest principal shear stress and $(\max \tau)^*$ the largest principal shear stress in the domain. This result, by the way, is in line with an old analytical solution by Sneddon [52], who investigated stresses around a Griffith crack in an elastic medium.

With an increasing pore pressure, the notch starts to open and the crack evolves horizontally, see Fig. 5 displaying the evolution of the phase field ϕ^S in (a)–(c) and the corresponding pore pressure in (d)–(f). After having applied the pore pressure $\bar{p}$, one observes a more or less radial pressure distribution around the notch. This also indicates the pore-fluid flow perpendicular to the pressure isolines towards the permeable boundaries. With an evolving phase field, the pressure isolines change their directions, and the pressure gradient along the crack is much smaller than perpendicular to it. The reason for this behaviour is obvious and can be found in the shrinking flow resistance along the crack. This can also be concluded from the fluid momentum balance included in Table 1, together with the constitutive equations (34)$_{2,3}$, indicating that the momentum production $\hat{\mathbf{p}}_E^F$ decreases while the friction force div $\mathbf{T}_E^F$ increases with the increasing phase field variable ϕ^S. However, note in passing that the friction force is generally quite small as a result of small velocity gradients along the notch.

The scaled norm

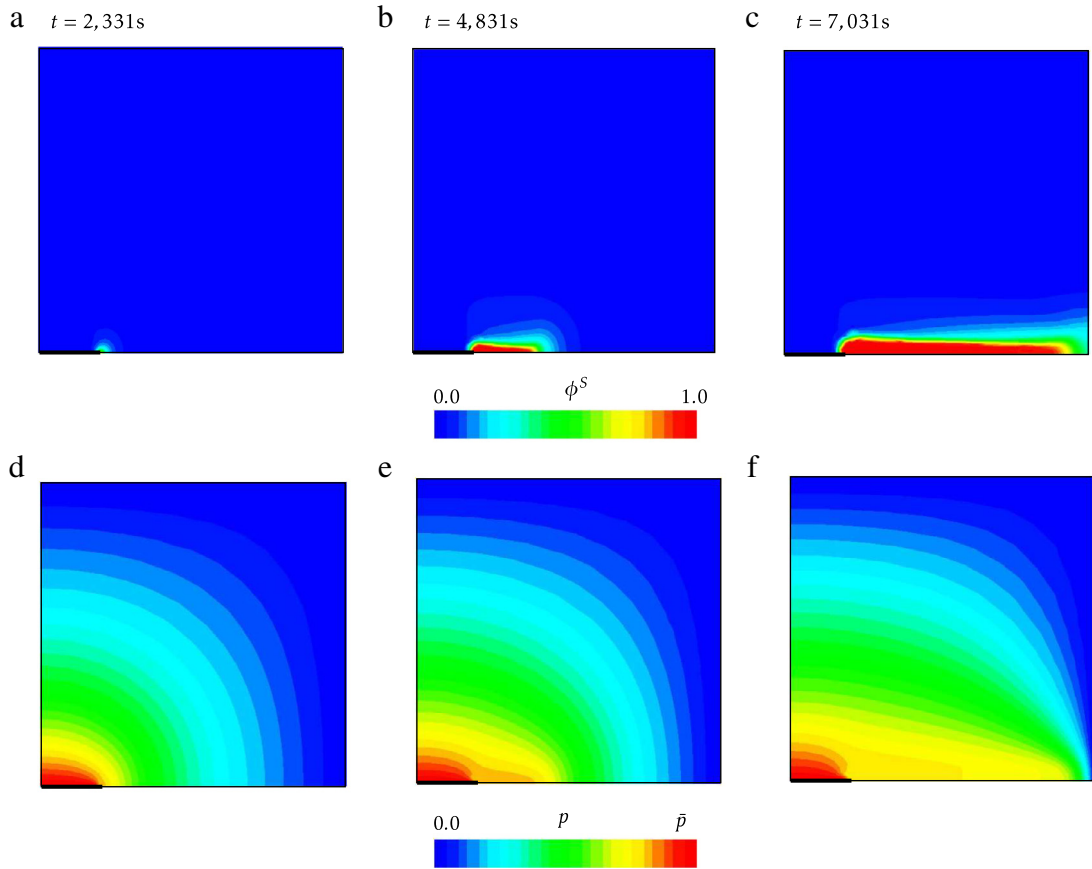$$v^* = \log_{10} \left(\frac{|\mathbf{v}_F|}{\min |\mathbf{v}_F|} \right) \tag{47}$$

Fig. 5. Phase field ϕ^S (a)–(c) and pore-fluid pressure p (d)–(e) at the different time steps.
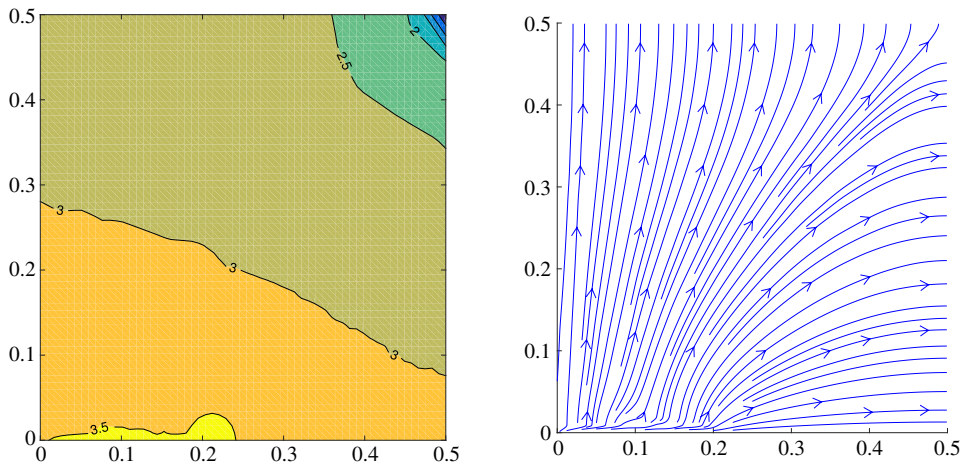

Fig. 6. (left) Contours of the scaled velocity norm v^*; (right) streamlines of the pore-fluid flow, both taken at $t = 4831$ s.

of the pore-fluid velocity together with the streamlines at $t = 4831$ s can be taken from Fig. 6. When computing v^*, min $|\mathbf{v}_F|$ is the minimum of the norm of the fluid velocity for each time step over the whole space domain. Furthermore, it is found that the fluid at $v^* = 4$ in the vicinity of the crack flows 100 times faster than at $v^* = 2$ in the top-right corner, cf. Fig. 6 (left). From the streamlines of Fig. 6 (right), one recognises that the flow follows two main directions. The one is the pore-fluid flow that starts perpendicular to the notch and the crack, and the other
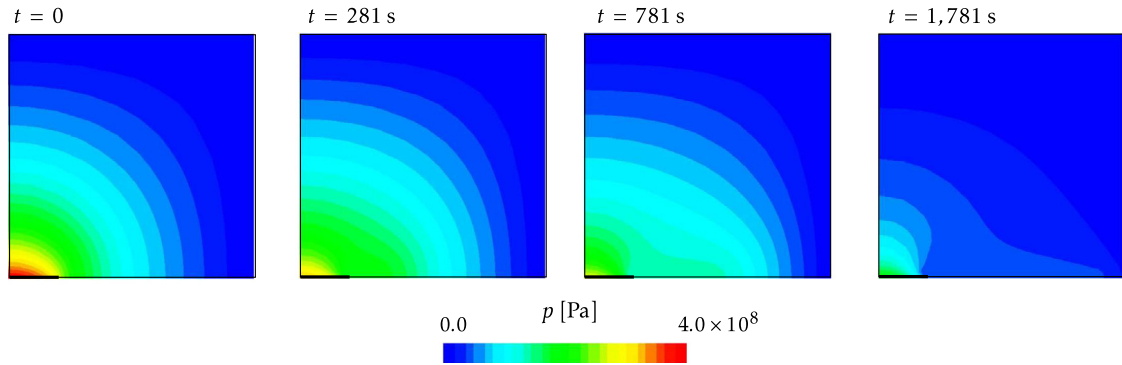
Fig. 7. Pressure distribution under a constant fluid influx at various times t.

is the bulk flow along the crack propagation. The breaking point, where the pore-fluid flow transforms towards the bulk-fluid flow, naturally coincides with the crack tip.

Proceeding from a pressure-driven crack propagation, attention has to be paid to the point, when the crack approaches the permeable surface. Here, the problem occurs that the pressure drop in the cracked zone is rather small, that means, p is approximately in the order of the loading pressure $\bar{p}$, while the boundary is stress-free. As a result, the computation tends towards a singularity in the pressure field, when the crack approaches the boundary. In this regard, Fig. 8(a) reveals a sudden drop of the resultant solid force at the top bearing at approximately $t = 7000$ s after having started the loading by $\bar{p}$. From this point on, the crack propagates only very slowly due to convergence problems. To overcome this situation, the loading has been changed from pressure-driven to influx-driven by an amount of $\bar{v} = 0.0025$ m^3/(m^2 s). This leads to the pressure contours of Fig. 7.

In this case, no singularity problem has to be expected due to the $p_0 = 0$ boundary condition, since the pressure at the tip of the notch has approximately the same value like the ambient pressure, when the crack penetrates the boundary at $t = 1781$ s. Thus, this case is convenient for further parameter studies. Varying the hydraulic conductivity, cf. Fig. 8(b), one observes a strong dependency of the resultant vertical solid force on k^F, especially, during the first 200 s of the loading. Since k^F governs the coupling between the solid deformation and the fluid flow through $\hat{\mathbf{p}}^F$, its importance on the vertical solid reaction force decreases after the specimen is pumped up by water. On the other hand, a variation of μ^{FR} does not show any influence on solid force. Since μ^{FR} governs the frictional fluid stress $\mathbf{T}_E^F$ in the cracked zone, it is again concluded that this effect is of minor importance for the overall fracking process. In addition, a variation of the length-scale parameter ϵ clearly shows that this quantity is most important for the overall computation of the problem, cf. Fig. 8(d). Since ϵ indirectly governs the thickness of the crack, it also governs the permeability of the cracked zone. As a result, larger values of ϵ lead to an increasing thickness of the crack and, in turn, to a faster outflow of the pumped-in water. Vice versa, smaller values of ϵ do the opposite and obviously yield a greater portion of the pumped-in water to choose its way through the porous solid, thus inducing higher and longer lasting high values of the vertical solid reaction force. Finally, the influence of the mobility parameter M is shown in Fig. 8(e), where several values of M are tested over a large range from 3×10^3 to 3×10^8 N s/m^2. When M is less than 3×10^6 N s/m^2, no significant deviation is found in the resultant solid reaction force. The reason is apparent if the phase-field evolution equation is rearranged as

$$M(\phi^S)'_S - 2(1 - \phi^S)\mathcal{H} + \frac{G_c}{\epsilon}(\phi^S - \epsilon^2 \operatorname{div} \operatorname{grad} \phi^S) = 0 \qquad (48)$$

and the order of each term is compared. As the values of $\mathcal{H}$ and G_c/ϵ are in the range of 10^6–10^7 J/m^3, the viscous term $M(\phi^S)'_S$ is negligible with M smaller than 10^6 Ns/m^2. Given the case that M is large enough, an increase of M results in a delay of crack nucleation and propagation, which yields a larger maximum and more gradual decrease of the vertical reaction force of the solid.

4.3. Hydraulic fracturing in 3 dimensions

In this section, a fully three-dimensional fracking problem is discussed. In particular, a liquid-saturated cylindrical specimen of permeable rock with outer radius $R_1 = 1$ m and height $H_1 = 1$ m is considered to be fixed between two
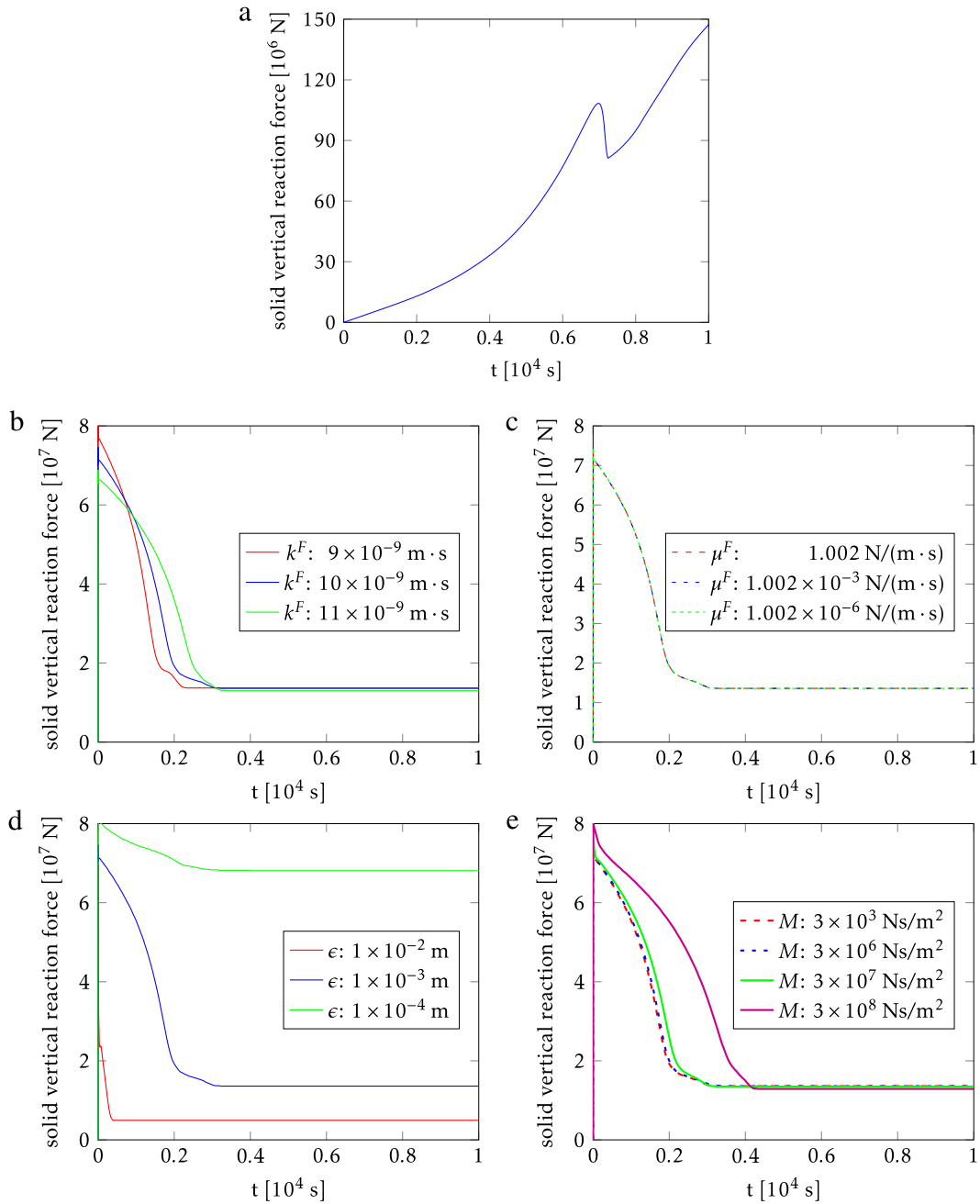
Fig. 8. Vertical resultant solid reaction force at the top bearing versus time: (a) pressure-driven case, (b)–(e) volume-injection-driven case with different parameter settings.

plates at the top and at the bottom. A borehole of radius $R_0 = 0.1$ m and height $H_0 = 0.5$ m is drilled into the centre of the upper part, cf. Fig. 9, in which a rigid and impermeable pipe is injected and fixed to the porous cylinder, such that a fluid injection can only be carried out through the bottom outlet of the pipe. The specimen is loaded by a prescribed liquid injection rate of 0.05 m^3/(m^2 s) at the bottom of the borehole. The boundary conditions are chosen in such a way that the cylinder cannot move upwards and downwards but freely expand to the sides, which are assumed to be impermeable as is the top surface. This means that an injected fluid can only blow up the specimen or escape through the permeable bottom surface which is subjected to a $p_0 = 0$ boundary condition. Due to symmetry reasons
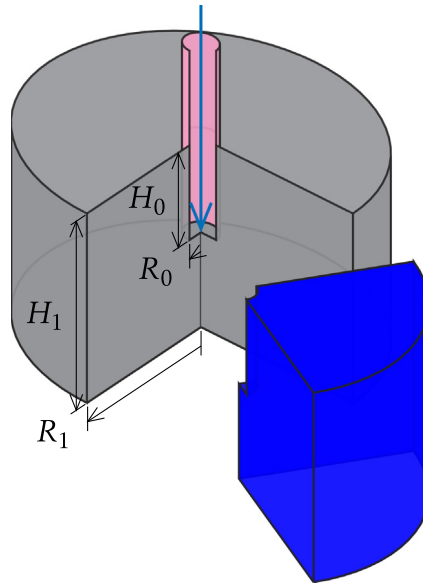
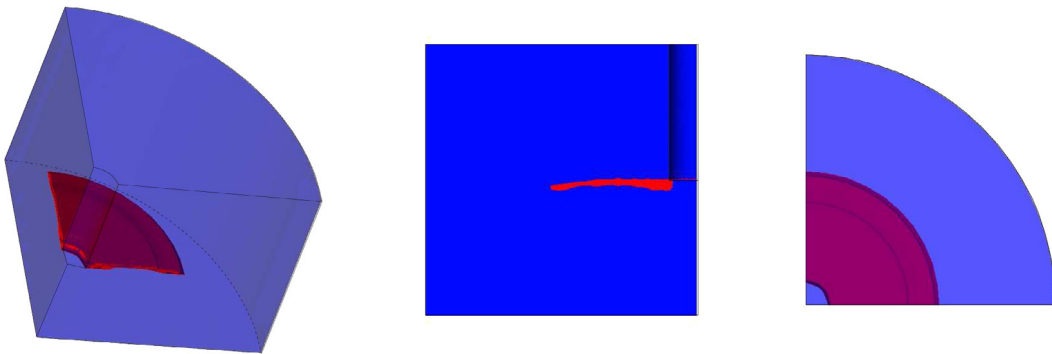Fig. 9. Geometry of the three-dimensional fracturing model.

Fig. 10. Crack surface in spatial, side and top view (For interpretation of the references to colour in this figure legend, the reader is referred to the web version of this article.)

and numerical efficiency, the numerical computation is set up for only one quarter of the specimen with symmetry boundary condition at the sides. By use of 2350 quadrilateral *Taylor–Hood* elements, the problem results in 11,118 nodes. After having fixed the essential boundary conditions, this results in 105,636 degrees of freedom. The minimum mesh size of $h^e \approx 0.01$ m is chosen at the vicinity of the outlet of the pipe, while the parameters for the computation are again taken from Table 4 as before.

Fig. 10 shows the crack surface in different views, where the red-coloured parts indicated the cracked zone with $\phi^S > 0.9$. While the spatial and the top view exhibit the extension of the cracked zone, the side view provides an insight in the local width of the fractured area, which is constant in circumferential direction as a result of radial symmetry. Since a fracking problem in a porous material has been considered, the liquid influx generates a pore-fluid flux with streamlines as shown in Fig. 11. These streamlines are a result of influx and boundary conditions as well as of the evolving cracked zone. One can observe that one part of the pore fluid flows directly downwards to the permeable bottom boundary, while the remainder of the influx mainly follows the cracked zone as a bulk fluid and enters the porous solid perpendicular to the cracked area, before it follows its way downwards to the bottom boundary. At the same time, the specimen extends volumetrically as a result of pore pressure.
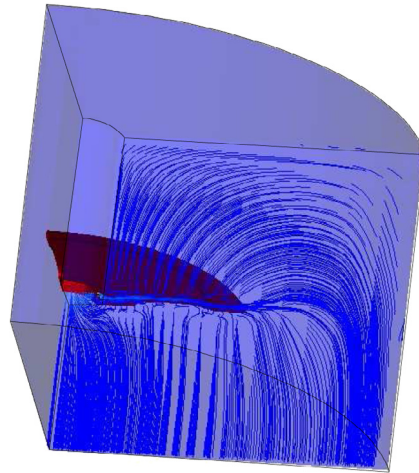
Fig. 11. Stream lines of the injected pore fluid.

5. Conclusion

Embedding the phase-field approach to fracture in the TPM opens a new possibility for the study and the computation of dynamic hydraulic fracturing problems. While the TPM guarantees thermodynamic consistency of the coupled behaviour of solid deformation and pore-fluid flow including the phase-field evolution, the phase-field approach to fracture exhibits an efficient way to include fluid-injection-induced brittle fracture in the standard description of porous media.

The present study makes use of an inclusion of the phase-field variable in the constitutive description of the solid material and of the pore-fluid flow, such that a weakening of the solid as well as an automatic switch between pore-fluid and bulk fluid conditions is obtained in cracked areas. Numerical benchmark problems for a single solid and for fluid-saturated porous media under two and three spatial dimensions furthermore exhibit the capabilities of PANDAS when multi-physical and multi-phasic problems have to considered. In this regard, it should be mentioned that PANDAS, if necessary, can also easily be coupled to commercial tools such as Abaqus, when numerically high-dimensional or large-scale problems have to be considered, for example, by parallel computing techniques.

Acknowledgements

References

[1] Z.P. Bažant, M. Salviato, V.T. Chau, H. Viswanathan, A. Zubelewicz, Why fracking works, J. Appl. Mech. 81 (2014) 101010.
[2] A.A. Griffith, The phenomena of rupture and flow in solids, Philos. Trans. R. Soc. Lond. Ser. A (1921) 163–198.
[3] G.R. Irwin, Analysis of stresses and strains near the end of a crack traversing a plate, J. Appl. Mech. 24 (1957) 361–364.
[4] J.R. Rice, A path independent integral and the approximate analysis of strain concentration by notches and cracks, J. Appl. Mech. 35 (1968) 379–386.
[5] G.I. Barenblatt, The mathematical theory of equilibrium cracks in brittle fracture, Adv. Appl. Mech. 7 (1962) 55–129.
[6] D. Dugdale, Yielding of steel sheets containing slits, J. Mech. Phys. Solids 8 (1960) 100–104.
[7] L.M. Kachanov, Time of the rupture process under creep conditions, Izv. Akad. Nauk SSSR Otd. Tekh. Nauk 8 (1958) 26–31.
[8] D. Gross, T. Seelig, Fracture Mechanics With an Introduction to Micromechanics, second ed., Springer-Verlag, Berlin, 2011.
[9] J. Lemaitre, A Course on Damage Mechanics, Springer-Verlag, Berlin, 1996.
[10] T. Belytschko, T. Black, Elastic crack growth in finite elements with minimal remeshing, Internat. J. Numer. Methods Engrg. 45 (1999) 601–620.

[11] N. Moës, T. Belytschko, Extended finite element method for cohesive crack growth, Eng. Fract. Mech. 69 (2002) 813–833.

[12] N. Moës, J. Dolbow, T. Belytschko, A finite element method for crack growth without remeshing, Internat. J. Numer. Methods Engrg. 46 (1999) 131–150.

[13] M.E. Gurtin, Generalized Ginzburg-Landau and Cahn-Hilliard equations based on a microforce balance, Physica D 92 (1996) 178–192.

[14] G.A. Francfort, J.J. Margio, Revisting brittle fracture as an energy minimization problem, J. Mech. Phys. Solids 46 (1998) 1319–1342.

[15] C. Kuhn, R. Müller, A continuum phase field model for fracture, Eng. Fract. Mech. 77 (2010) 3625–3634.

[16] M.J. Borden, C.V. Verhoosel, M.A. Scott, T.J. Hughes, C.M. Landis, A phase-field description of dynamic brittle fracture, Comput. Methods Appl. Mech. Engrg. 217 (2012) 77–95.

[17] C. Miehe, M. Hofacker, F. Welschinger, A phase field model for rate-independent crack propagation: Robust algorithmic implementation based on operator splits, Comput. Methods Appl. Mech. Engrg. 199 (2010) 2765–2778.

[18] M. Jirásek, Nonlocal theories in continuum mechanics, Acta Polytech. 44 (2004) 16–34.

[19] R. de Boer, Theory of Porous Media: Highlights in Historical Development and Current State, Springer-Verlag, Berlin, 2000.

[20] W. Ehlers, Porous media in the light of history, in: E. Stein (Ed.), The History of Theoretical, Material and Computational Mechanics – Mathematics Meets Mechanics and Engineering, in: Lecture Notes in Applied Mathematics and Mechanics, vol. 1, Springer, Heidelberg, 2014, pp. 211–227.

[21] M.A. Biot, General theory of three-dimensional consolidation, J. Appl. Phys. 12 (1941) 155–164.

[22] M.A. Biot, Theory of propagation of elastic waves in a fluid-saturated porous solid, I. Low frequency range, J. Acoust. Soc. Am. 28 (1956) 168–178.

[23] M.A. Biot, Theory of propagation of elastic waves in a fluid-saturated porous solid, II. Higher frequency range, J. Acoust. Soc. Am. 28 (1956) 179–191.

[24] R.M. Bowen, Incompressible porous media models by use of the theory of mixtures, Internat. J. Engrg. Sci. 18 (1980) 1129–1148.

[25] R.M. Bowen, Compressible porous media models by use of the theory of mixtures, Internat. J. Engrg. Sci. 20 (1982) 697–735.

[26] R. de Boer, Highlights in the historical development of the porous media theory: Toward a consistent macroscopic theory, Appl. Mech. Rev. 49 (1996) 201–262.

[27] R. de Boer, Theory of Porous Media, Springer-Verlag, Berlin, 2000.

[28] W. Ehlers, Constitutive equations for granular materials in geomechanical context, in: K. Hutter (Ed.), Continuum Mechanics in Environmental Sciences and Geophysics, in: CISM Courses and Lectures, vol. 337, Springer-Verlag, Wien, 1993, pp. 313–402.

[29] W. Ehlers, Foundations of multiphasic and porous materials, in: W. Ehlers, J. Bluhm (Eds.), Porous Media: Theory, Experiments and Numerical Applications, Springer-Verlag, Berlin, 2002, pp. 3–86.

[30] C. Truesdell, R.A. Toupin, The classical field theories, in: S. Flügge (Ed.), in: Handbuch der Physik, vol. III/1, Springer-Verlag, Berlin, 1960, pp. 226–902.

[31] R.M. Bowen, Theory of mixtures, in: A.C. Eringen (Ed.), in: Continuum Physics, vol. III, Academic Press, New York, 1976, pp. 1–127.

[32] W. Ehlers, B. Markert, A linear viscoelastic biphasic model for soft tissues based on the theory of porous media, J. Biomech. Eng. 123 (2001) 418–424.

[33] W. Ehlers, Challenges of porous media models in geo- and biomechanical engineering including electro-chemically active polymers and gels, Int. J. Adv. Eng. Sci. Appl. Math. 1 (2009) 1–24.

[34] N. Karajan, Multiphasic intervertebral disc mechanics: Theory and application, Arch. Comput. Methods Eng. 19 (2012) 261–339.

[35] H.-U. Rempler, Damage in Multi-Phasic Materials Computed With The Extended Finite-Element Method (Dissertation thesis). Report No. II-23, Institute of Applied Mechanics (CE), University of Stuttgart, 2012.

[36] T.J. Boone, A.R. Ingraffea, A numerical procedure for simulation of hydraulically-driven fracture propagation in poroelastic media, Int. J. Numer. Anal. Methods Geomech. 14 (1990) 27–47.

[37] T.J. Boone, E. Detournay, Response of a vertical hydraulic fracture intersecting a poroelastic formation bounded by semi-infinite impermeable elastic layers, Int. J. Rock Mech. Min. Sci. Geomech. Abstr. 27 (1990) 189–197.

[38] E. Detournay, Propagation regimes of fluid-driven fractures in impermeable rocks, Int. J. Geomech. 4 (2004) 35–45.

[39] A. Mikelić, M.F. Wheeler, T. Wick, A phase field approach to the fluid filled fracture surrounded by a poroelastic medium, ICES Report, 2013, pp. 13–15.

[40] A. Mikelić, M.F. Wheeler, T. Wick, Phase-field modeling of pressurized fractures in a poroelastic medium, ICES Report, 2014, pp. 14–18.

[41] C. Miehe, S. Mauthe, Phase field modeling of fracture in multi-physics problems. Part III. Crack driving forces in hydro-poro-elasticity and hydraulic fracturing of fluid-saturated porous media, Comput. Methods Appl. Mech. Engrg. 304 (2015) 619–655.

[42] C. Miehe, S. Mauthe, S. Teichtmeister, Minimization principles for the coupled problem of Darcy-Biot-type fluid transport in porous media linked to phase field modeling of fracture, J. Mech. Phys. Solids 82 (2015) 186–217.

[43] B. Markert, Y. Heider, Coupled multi-field continuum methods for porous media fracture, in: M. Mehl, M. Bischoff, M. Schäfer (Eds.), Recent Trends in Computational Engineering — CE2014, in: Lecture Notes in Computational Science and Engineering, vol. 105, 2015, pp. 167–180.

[44] W. Ehlers, On thermodynamics of elasto-plastic porous media, Arch. Mech. 41 (1989) 73–93.

[45] W. Ehlers, P. Ellsiepen, P. Blome, D. Mahnkopf, B. Markert, Theoretische und numerische Studien zur Lösung von Rand- und Anfangswertproblemen in der Theorie Poröser Medien, Abschlußbericht zum DFG-Forschungsvorhaben Eh 107/6-2, Bericht aus dem Institut für Mechanik (Bauwesen), Nr. 99-II-1, Universität Stuttgart, 1999.

[46] C. Miehe, F. Welschinger, M. Hofacker, Thermodynamically consistent phase-field models of fracture: Variational principles and multi-field FE implementations, Internat. J. Numer. Methods Engrg. 83 (2010) 1273–1311.

[47] H.-U. Rempler, C. Wieners, W. Ehlers, Efficiency comparison of an augmented finite element formulation with standard return mapping algorithms for elastic-inelastic materials, Comput. Mech. 48 (2011) 551–562.

[48] B. Markert, Y. Heider, W. Ehlers, Comparison of monolithic and splitting solution schemes for dynamic porous media, Internat. J. Numer. Methods Engrg. 82 (2010) 1341–1383.

[49] W. Ehlers, S. Zinatbakhsh, B. Markert, Stability analysis of finite difference scheme revisited: A study of decoupled solution strategies for coupled multifield problems, Internat. J. Numer. Methods Engrg. 94 (2013) 758–786.

[50] C.A. Felippa, K.C. Park, Synthesis tools for structural dynamics and partitioned analysis of coupled systems, in: A. Ibrahimbegovic, B. Brank (Eds.), Engineering Structures Under Extreme Conditions: Multi-Physics and Multi-Scale Computer Models in Non-Linear Analysis and Optimal Design, IOS Press, Amsterdam, 2005, pp. 50–110.

[51] M. Hofacker, A Thermodynamically Consistent Phase Field Approach to Fracture (Dissertation thesis). Report No. I-29, Institute of Applied Mechanics (CE), University of Stuttgart, 2014.

[52] I.N. Sneddon, The distribution of stress in the neighbourhood of a crack in an elastic solid, Proc. R. Soc. Lond. A 187 (1946) 229–260.